Journal of Power Sources 206 (2012) 454–462

Contents lists available at SciVerse ScienceDirect

Journal of Power Sources

journal homepage: www.elsevier.com/locate/jpowsour

In situ crystallographic investigations of charge storage mechanisms in MnO_2-based electrochemical capacitors

Ouassim Ghodbane[a,b,*], Fatemeh Ataherian[c], Nae-Lih Wu[c], Frédéric Favier[a]

[a] Institut Charles Gerhardt, UMR 5253 CNRS, Université Montpellier 2, 34095 Montpellier cedex 05, France
[b] Institut National de Recherche et d'Analyse Physico-Chimique, Laboratoire des Matériaux Utiles, Pôle Technologique de Sidi Thabet, 2020 Sidi Thabet, Tunisia
[c] Department of Chemical Engineering, National Taiwan University, Taipei 106, Taiwan

ARTICLE INFO

Article history:
Received 11 October 2011
Received in revised form 15 January 2012
Accepted 16 January 2012
Available online 25 January 2012

Keywords:
In situ X-ray diffraction
Synchrotron
Manganese dioxides
Supercapacitor
Charge–discharge mechanism
Microstructural material changes

ABSTRACT

Structural behaviors of four MnO_2 allotropes are investigated by in situ synchrotron X-ray diffraction analyses upon charge/discharge cycling in LiCl and KCl aqueous media. During the anodic/cathodic scans of the 2D birnessite electrode, the interlayer spacing respectively extend/contract along the *z* direction by ~0.2 Å. This behavior is associated to electrostatic attractive forces between charged framework layers and hydrated electrolyte cations. In contrast, the oxidation/reduction of the 3D spinel electrode lead to the contraction/swelling of (1 1 1) crystalline planes by ~0.05 Å. Manganese–oxygen distance changes induced by Mn(III)/Mn(IV) redox reactions are assigned to such a mechanism. Structural characterizations are focused on the (0 0 2), (2 1 1), (1 1 0) and (2 0 0) planes for MnO_2 cryptomelane, while (0 0 2) and (2 0 0) planes for MnO_2 OMS-5. The 1D cryptomelane and OMS-5 electrodes also exhibit contraction/swelling processes of their structures upon discharge/charge cycling associated to deintercalation/intercalation of hydrated electrolyte cations in their channels, respectively, driven by size/steric constraints.

1. Introduction

Electrochemical supercapacitors are gaining more interest as complementary charge storage devices in various applications that especially require peak power pulses [1–5]. Numerous compounds were investigated as possible supercapacitor materials and manganese dioxides are certainly among the most attractive candidates [5–7]. This is mainly due to their low cost, environmental compatibility and appropriate electrochemical performances [8–10]. The chemistry of MnO_2 is abundant with a variety of structural types [11]. In the field of supercapacitors, the structural complexities exhibited by the 1D, 2D or 3D arrangement of MnO_2 materials result in various charge-storage performances [12]. It was recently demonstrated that, in contrast with the usual assumption, the electrochemical performance of MnO_2 based electrodes was not dependent on the specific surface area neither on the electronic conductivity [12]. However, among a series of seven distinct MnO_2 allotropes including 1D pyrolusite, ramsdellite, cryptomelane, Nitodorokite and Octahedral Molecular Sieves (OMS-5), 2D birnessite and 3D spinel, specific capacitances were found to strongly correlate with the corresponding ionic conductivity, which obviously rely on the microstructure and more precisely on cavity size and connectivity. It was also shown that the specific capacitance of MnO_2 is enhanced with the dimensionality of the structure from the 1D to 3D arrangements, while in the 1D group the highest capacitance was reached with the largest channel size [12]. Moreover, Brousse et al. showed that the material bulk of birnessite-like MnO_2 mostly contributes to the electrochemical performance, and that its crystalline microstructure leads to insertion/extraction processes of cations present in the electrolyte solution [13]. Nevertheless, studies dealing with the microstructure behaviors during the charge storage process of MnO_2-based electrodes are rather scarce [14–16]. The insertion/extraction of protons (H^+) and electrolyte cations (C^+) into/from the bulk structures involved during the charge/discharge of MnO_2-based electrodes may be described by the following reactions [6,17]:

$$MnO_2 + H^+ + e^- \leftrightarrow MnOOH \quad (1)$$

$$MnO_2 + C^+ + e^- \leftrightarrow MnOOC \quad (2)$$

where $C^+ = K^+, Li^+$.

Using synchrotron X-ray diffraction measurements on a disordered structure close to Akhtenskite (ε-MnO_2), Kuo and Wu found the *d*-spacings of all reflections to expand upon the cathodic scan (charge process), while they all contract during the anodic scan (discharge process) [6]. This reversible swelling was definitively assigned to volumetric/steric origins and namely the insertion

* Corresponding author at: Institut National de Recherche et d'Analyse Physico-Chimique, Laboratoire des Matériaux Utiles, Pôle Technologique de Sidi Thabet, 2020 Sidi Thabet, Tunisia. Tel.: +216 71537666; fax: +216 71537688.
E-mail addresses: ouassim.ghodbane@inrap.rnrt.tn (O. Ghodbane), fredf@um2.fr (F. Favier).

0378-7753/$ – see front matter © 2012 Elsevier B.V. All rights reserved.
doi:10.1016/j.jpowsour.2012.01.103

(respectively desinsertion) of hydrated alkali cations from the electrolyte into the lattice to cause the swelling (respectively contraction) as charge changes induced by Mn(IV)/Mn(III) redox reactions are balanced thanks to the electrolyte cations [6]. Accordingly, such a structural breathing was expected to be universal to all crystallographic directions, and it was indeed observed to be so [6].

The scope of the present paper is to get a better insight into the origin of these experimental evidences by performing in situ synchrotron X-ray diffraction studies on four MnO_2 allotropes: cryptomelane, OMS-5, birnessite and spinel. Diffraction data collected during the electrochemical charge/discharge of these MnO_2-based electrodes are aimed to assign eventual pattern feature changes to microstructural transformations associated to the corresponding electrochemical mechanism and induced ion movements through the material structure. These four selected MnO_2 phases showed, in our previous work, remarkable electrochemical performances with capacitances at 125 $F g^{-1}$ for cryptomelane, 217 $F g^{-1}$ for OMS-5, 225 $F g^{-1}$ for birnessite and 241 $F g^{-1}$ for spinel [12]. As for other MnO_2 allotropes, their structures are built on MnO_6 octahedral units sharing corners and/or edges: MnO_2 cryptomelane and OMS-5 shows 2×2 and 2×4 1D channels, respectively. The birnessite form is a layered 2D structure while MnO_2 spinel is a compact 3D cubic structure. Despite these drastic differences in their structural arrangements (Fig. 1), capacitances were found in the same range as for their corresponding ionic conductivities. On the other hand, their corresponding cyclic voltammogram (CV) signatures display such specific features that the observed performances are suspected to originate from distinct electrochemical mechanisms. Although OMS-5 and cryptomelane are both sharing a 1D structure, their CVs are completely different, suggesting again distinct electrochemical mechanisms.

The present work presents a detailed study of the relationship between the electrochemical behaviors and the evolution of crystalline structures of MnO_2 birnessite, spinel, cryptomelane and OMS-5. Cyclic voltammetry (CV) experiments were used to investigate the electrochemical properties of MnO_2-based electrodes. In situ synchrotron XRD measurements were performed at various oxidized and reduced stages of MnO_2 materials to follow their microstructural changes during charge/discharge cycles. The structural properties are also discussed in relation to the nature of the exchanged cations present in the pristine material as well as in the electrolyte aqueous solution.

2. Experimental

All chemical reagents were analytical grade and have been used as purchased without further purification. Several techniques were employed in order to prepare a set of manganese dioxides showing various microstructures. The synthesis methods are described below. All aqueous solutions were prepared using de-ionized water (18 MΩ, obtained from an ELGALabWater de-ionized system).

2.1. Synthesis of MnO_2 Na-birnessite [18]

An aqueous solution (A) was prepared by dissolving 0.04 mol of $KMnO_4$ (99%, Aldrich) and 1.2 mol of NaOH (ACS grade, VWR) in 400 mL of water. Afterward, another aqueous solution (B) was prepared by dissolving 0.112 mol of $MnCl_2{\cdot}4H_2O$ (99%, Aldrich) in 400 mL of water. Solution B was added dropwise to solution A with vigorous stirring in an ice bath. The resulting precipitate was statically aged at room temperature for 1 day and then washed and dried at 90 °C.

2.2. Synthesis of MnO_2 Na-cryptomelane [19]

The cryptomelane powder was prepared from the ignition in air of MnO_2 Na-birnessite at 400 °C for 60 h.

2.3. Synthesis of MnO_2 Na-OMS-5 [18]

The Na-birnessite powder (0.5 g) was autoclaved at 180 °C for 2 days with 100 mL of 0.1 M NaOH aqueous solution giving the title compound.

2.4. Synthesis of MnO_2 H-spinel [13]

Firstly, as MnO_2 spinel precursor, $LiMn_2O_4$ was prepared as follows: $LiNO_3$ (99%, Fisher Scientific) and $Mn(NO_3)_2{\cdot}2H_2O$ (ACS grade, Fisher Scientific) (molar ratio 1:2) were dissolved in a mixture of citric acid (ACS grade, Aldrich) and ethylene glycol (ACS grade, Aldrich) (molar ratio 1:4). The solution was heated at 90 °C for 30 min and the temperature was subsequently increased to 140 °C in order to trigger esterification and remove the ethylene glycol excess. This solution was heated at 180 °C under vacuum and a pale brown powder was obtained. The resulting powder was annealed at 250 °C in air leading to $LiMn_2O_4$. Finally, the spinel phase was synthesized by hydrolyzing $LiMn_2O_4$ in a 0.5 M HCl (ACS grade, Aldrich) aqueous solution for 24 h at ambient temperature.

2.5. Preparation of electrodes and XRD characterization

The electrodes for synchrotron XRD analyses were made of the mixture of MnO_2 particles and conductive carbon black (VULCAN XC72, Cabot Corp., USA) with a weight ratio of 8:2. Poly(tetrafluoroethylene) (PTFE) (5 wt%) was used as the binder and Ti mesh was used as the current collector. The electrodes were finally dried at 120 °C for 6 h in vacuum. Analyses were conducted with the beam line 01-C2 facilities of the National Synchrotron Radiation Research Center (NSRRC) in Taiwan.

The synchrotron XRD instrument setup is shown in Fig. A.1a, and the construction of the electrochemical cell for the in situ study is illustrated in Fig. A.1b. The main body of the cell was made of acrylics, and the two sides of the cell were perforated and then sealed with Kapton foils in order to allow the probing beam to pass through the cell. The X-ray wavelength of 0.0775 nm was used. The patterns were acquired during the course of a cyclic voltammetric scan running at a scan rate of 0.2 mV s^{-1} between 0.0 and 1.0 V (vs Ag/AgCl/sat. $KCl_{(aq)}$), and they were recorded by a curved translating imaging plate (Fuji BAS2500) with the sample-to-film distance of 280 mm. Two-dimensional data were converted using the FIT2D program.

3. Results and discussion

3.1. Crystallographic microstructures

Crystallographic structures of studied MnO_2 phases are depicted in Fig. 1. XRD measurements were used as a qualitative tool for phase identification (Fig. A.2). The identification of crystalline systems, space groups and lattice parameters of each prepared MnO_2 phase was previously detailed [12]. In the present work, in situ synchrotron XRD characterizations will focus on the peak series among all reflections of each MnO_2 powder, showing changing diffraction characteristics (d-spacing) upon voltammetric cycling. As an example of resulting data, Fig. 2 depicts a series of diffraction patterns taken in situ using 1 M LiCl as supporting electrolyte and showing the reversible shift of the MnO_2-birnessite (0 0 1) peak at various charge/discharge states. On the other hand, some other peaks experiencing any changes can eventually be identified and assigned to

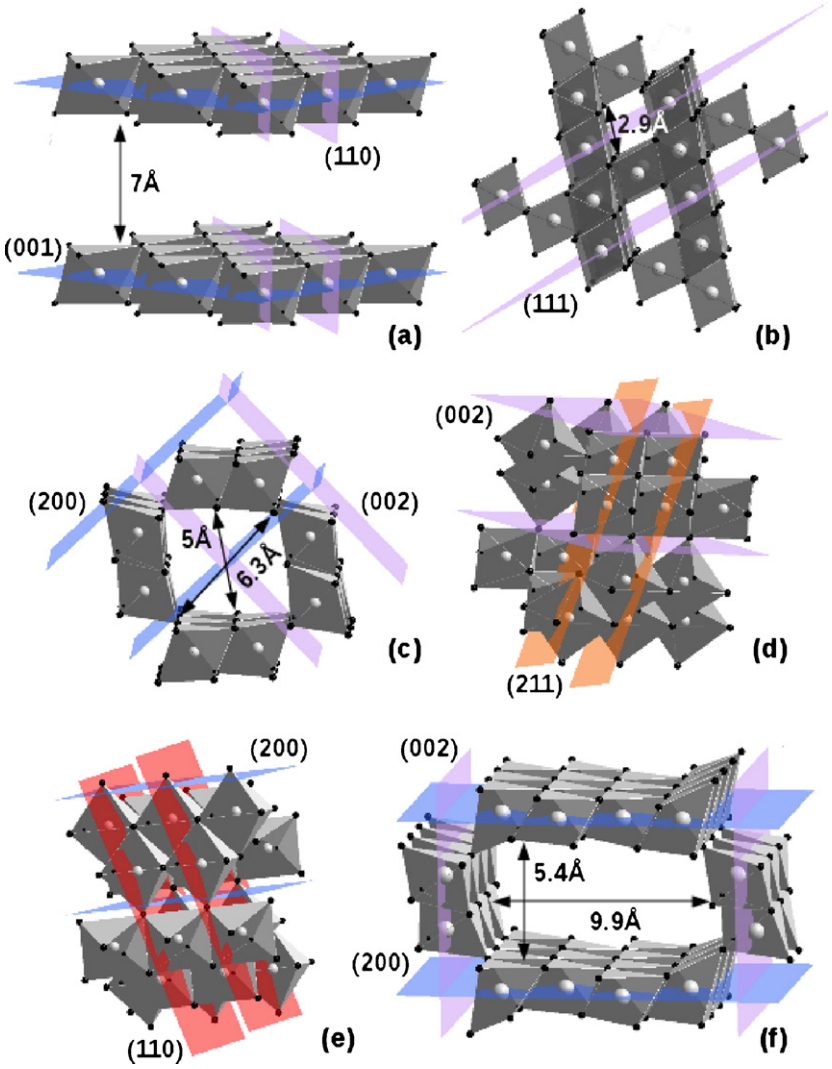

Fig. 1. Crystallographic structures of MnO_2 birnessite (a), spinel (b), cryptomelane (c–e) and OMS-5 (f) together with selected characteristic crystal planes and distances.

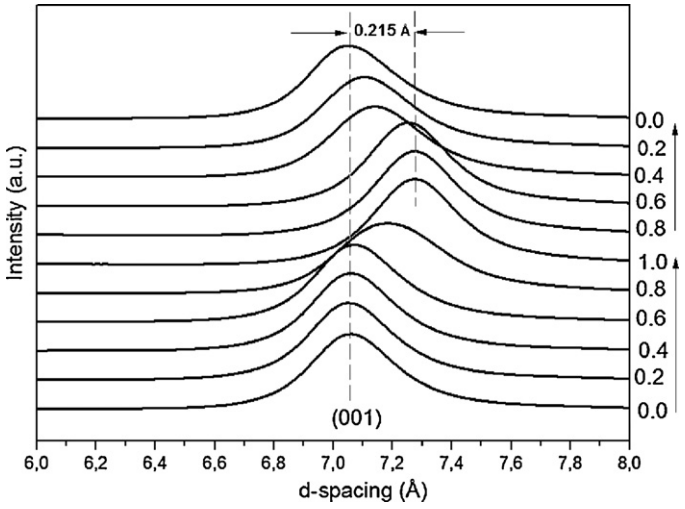

Fig. 2. Evolution of the (0 0 1) Bragg peak of MnO_2 birnessite-based electrode during the course of a CV scan in 1 M LiCl. The potential was stopped at each of the indicated values for 2 min for data collection.

plane distances remaining upon cycling. These latter will not be discussed in the next sections. For MnO_2 birnessite (Fig. 1a), the study of the 2D layered structure is then based on the (0 0 1) and (1 1 0) reflections planes. The structural investigation of 3D interconnected tunnels of MnO_2 spinel (Fig. 1b) is carried out following the (1 1 1) peak. The study of the 1D channels arrangement of MnO_2 cryptomelane (Figs. 1c–e) and MnO_2 OMS-5 (Fig. 1f) are based on their corresponding (0 0 2) and (2 0 0) peaks. In the case of MnO_2 cryptomelane, the peak follow-up also concerns the (1 1 0) and (2 1 1) diffractions (Fig. 1d and e).

3.2. Cyclic voltammetry results

CV curves of MnO_2-based electrodes measured in the in situ XRD setup in 1 M KCl and 1 M LiCl are presented in Fig. 3. Significant differences in behavior are observed for the four electrodes. The typical rectangular shape of pseudocapacitive behaviors, where the current flow is independent of the electrode potential, is observed for the spinel phase only in KCl electrolyte (Fig. 3a, red curve). In this case, the onsets of oxygen evolution and MnO_2-catalyzed oxygen reduction reaction are observed at the most positive and negative potentials, respectively. The broad peak located at 0.1 V on the anodic scan can be assigned to oxygen reduction catalyzed by the spinel [20–22]. The CV profile of MnO_2 spinel is slightly different

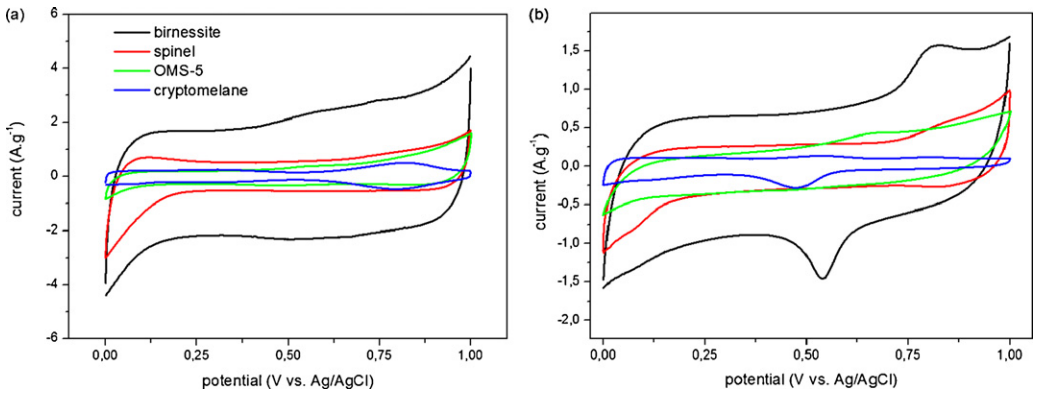

Fig. 3. CV curves of different MnO_2 composite electrodes recorded at 5 mV s^{-1} in aqueous 1 M KCl (a) and 1 M LiCl (b). (For interpretation of the references to color in the text, the reader is referred to the web version of the article.)

in LiCl electrolyte wherein redox waves, of low current intensities, are exhibited (Fig. 3b, red curve). In fact, quasi-reversible redox waves are observed at 0.84 V, in addition to a new cathodic wave appearing at about 0.1 V. The main difference in CV profiles should be related to the two distinct ionic radii of K^+ and Li^+ in crystals (K^+ radius > Li^+ radius) [23]. The reaction of MnO_2 electrodes in K^+ containing solutions was assumed to be a proton–electron mechanism due to the larger radius of K^+ in crystal [24]. While for Li^+ containing solutions, cation intercalation/deintercalation reaction can be envisioned [25]. The reaction of MnO_2 spinel electrode in LiCl solution should be considered as a reversible insertion/extraction of Li^+ in the small cavities with charge transfer at the electrode/electrolyte interface, as ascribed by the following reaction [25]:

$$MnO_2 + xLi^+ + xe^- \leftrightarrow Li_xMnO_2 \quad (3)$$

For the birnessite, cryptomelane, and OMS-5 electrodes, the shapes of CV curves exhibit more or less pronounced redox waves. In the presence of KCl electrolyte, the birnessite curve shows anodic and cathodic waves centered at about 0.60 and 0.52 V, respectively (Fig. 3a, black curve). They were associated to faradic reactions occurring during the charge storage mechanism [12]. Brousse et al. assigned the redox waves of layered manganese dioxides to the deintercalation of electrolyte cation upon Mn^{3+} oxidation and the cation intercalation upon Mn^{4+} reduction [13]. On the other hand, the birnessite curve recorded in the presence of LiCl electrolyte exhibit anodic and cathodic peaks at 0.82 and 0.54 V, respectively (Fig. 3b, black curve). The potential difference between the two peaks indicates the existence of energy barrier associated with the transformation between cation-rich and -lean domains within the oxide matrix. For the cryptomelane electrode in KCl electrolyte (Fig. 3a, blue curve), the CV curve shows two reversible redox anodic waves centered at 0.28 and 0.80 V (and corresponding cathodic waves at roughly the same potentials). However, in LiCl electrolyte, the cryptomelane curve indicates the presence of three anodic waves at 0.24, 0.54 and 0.80 V, while only two cathodic waves at 0.47 and 0.13 V (Fig. 3b, blue curve). These results suggest that the redox reaction mechanisms of MnO_2 cryptomelane in KCl and LiCl should be quite different. The CV curve of MnO_2 OMS-5 shows an anodic wave centered at about 0.57 and 0.65 V, in the presence of KCl and LiCl, respectively (Fig. 3a and b, green curve). When the potential is reversed, a cathodic hump is exhibited at 0.45 V in both electrolyte solutions. These waves, observed on the cryptomelane and OMS-5 curves, are assigned to reversible faradic reactions in the complex manganese redox system but precise assignations are still under investigation.

3.3. MnO_2 Na-birnessite

The formation of the 2D layered structure of MnO_2 Birnessite (JCPDS 43-1456) is confirmed by the presence of main peaks at *d*-spacings = 7.0 (0 0 1), 3.5 (0 0 2), 2.4 (1 1 0) and 1.4 Å (1 1 9) (Fig. A.2). As mentioned above, among these diffraction peaks, only the peaks corresponding to (0 0 1) and (0 0 2) reflection planes show *d*-spacing changes upon cycling while others, including the (1 1 0) peak (Figs. A.3 and A.4), remain unchanged. (0 0 1) and (1 1 0) peaks correspond to the interlayer distance along the *z* direction (*c* axis) and Mn-Mn distances from edge-sharing MnO_6 octahedra building the layer, respectively. For obvious reason, (0 0 2) *d*-spacing shifts will not be discussed. In contrast, Fig. 4 shows the evolution of the birnessite interlayer distance during the voltammetric cycling in 1 M LiCl (open circles) or KCl (plain circles) solution. The dashed line at 7.0 Å corresponds to the interlayer distance measured for the as prepared birnessite dry powder. The immersion of the electrode into the electrolyte solution results in an obvious swelling of the interlayer space at open circuit voltage (OCV). From dry state, the interlayer distance increases by +0.9% in aqueous LiCl and +1.3% in aqueous KCl. Such a behavior results from a spontaneous insertion of Li^+ or K^+ hydrated cations (and eventually Cl^- anions and H_2O molecules) in-between the layers. The interlayer distance in birnessite can then be considered as resulting from an electrostatic balance between negatively charged layers and intercalated hydrated cations. The interlayer spacing of the birnessite (>7 Å) is

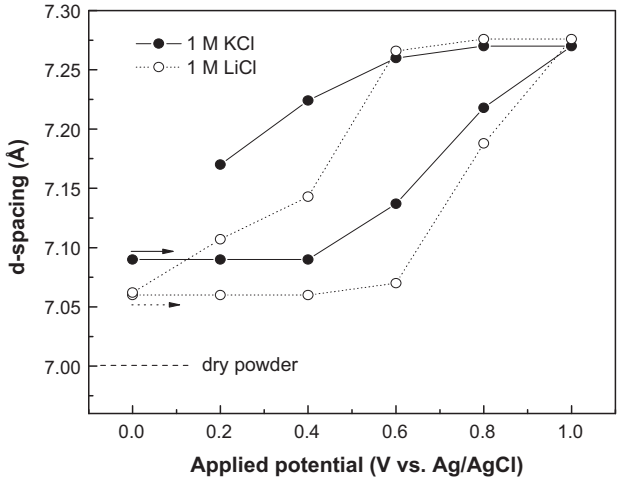

Fig. 4. Variation of the (0 0 1) Bragg peak of MnO_2 birnessite-based electrode during the course of a CV scan recorded in the presence of 1 M KCl or LiCl aqueous solutions.

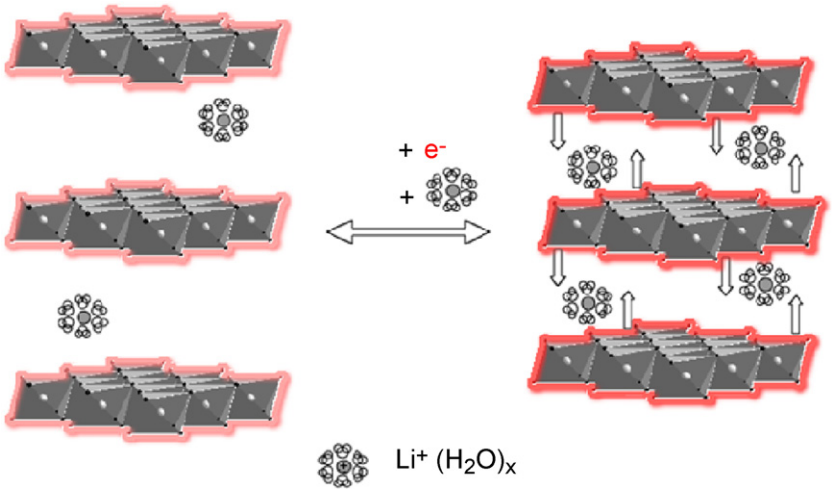

Fig. 5. Schematics showing the electrostatic effect of intercalated/deintercalated hydrated cations between MnO_2 layers in birnessite.

significantly larger than the sizes of proton (3.4 Å for H_3O^+) and alkali cations (2.25 Å for $Li(H_2O)_4$ and 2.92 Å for $K(H_2O)_4^+$ for 1M LiCl and KCl solutions respectively) [26] as well as water molecules (2.8 Å) from the electrolyte solution. Thus, there is enough space for species to move in and out within the layers.

As shown in Fig. 4, in both electrolytes, the (0 0 1) *d*-spacing increases with increasing the potential during the anodic scan (discharge process) and then contract back to its original value at the end of the cathodic scan (charge process). This strongly contrasts with the changes in the *d*-spacings observed in disordered Akhtenskite, which shows contraction upon discharge [6], but fits well with what was previously observed in birnessite-like layered MnO_2 materials [14,15]. In those cases, the changes were assigned to volumetric/steric origins associated to cation deintercalation/intercalation [6,16,27,28]. The existence of a reversible deintercalation/intercalation process of Na^+ cations from/into the birnessite lattice during electrochemical discharge/charge was demonstrated in aqueous electrolytes by energy dispersive X-ray (EDX) and ex situ X-ray diffraction [14,15]. Previous studies suggested that the decrease in Na^+ amount in the structure upon discharge is simultaneously compensated by the intercalation of H_2O molecules inducing an increase of the interlayer spacing [14,27,28]. In the same way, the increase in Na^+ amount in the structure observed upon reduction was associated to the desintercalation of H_2O molecules and consequently to the shrinkage of MnO_2 interlayer spacing [29,30].

Compared with literature data [14,15], the present observations on birnessite electrode behavior, especially its *d*-spacing variations, are believed to result from another origins. The average contraction for $\Delta V = 1.0$ V is about 0.2 Å (Fig. 4), which is considerably greater than the *d*-spacing variation that could arise from volumetric considerations, as observed elsewhere for Mg-doped Na-birnessite powder [14]. A schematic cartoon of the observed "breathing" of the birnessite structure is given in Fig. 5. As cations are intercalated into the space between MnO_2 layers during the cathodic scan (or charge process), increased overall electrostatic attraction forces cause the (0 0 1) *d*-spacing to contract. Because of the low electronic conductivity at 58×10^{-7} S cm^{-1} of birnessite (the lowest in the studied MnO_2 allotrope series) [12], the charge percolation is limited through the electrode material. The increase in the negative charge supported by the layers during the charge process enhances the observed electrostatic effect. On the other hand, the spacing expands during the anodic scan when cations between the layers are expelled out of the structure and negative charges on the layers decreases.

Nevertheless, some differences between KCl and LiCl electrolytes can be pointed out in Fig. 4: in KCl electrolyte solution, the maximum variation in *d*-spacing is relatively smaller in KCl (0.180 Å) than in LiCl solution (0.216 Å). This clearly confirms the charge storage mechanism in birnessite as electrostatically rather sterically driven: $K^+(H_2O)_4$ is larger than $Li^+(H_2O)_4$ (2.92 Å vs. 2.25 Å), and hence $K^+(H_2O)_4$ presents a smaller charge density, leading to smaller electrostatic attractive forces with MnO_2 layers.

On the other hand, in both electrolytes, the birnessite structure does not experience any structural changes at the beginning of both anodic and cathodic scans. (0 0 1) *d*-spacings remain at 7.06 Å and 7.09 Å in LiCl and KCl, respectively, up to 0.4–0.6 V and then strongly increase up to 7.27 Å at 1 V during the anodic scan. At the beginning of the cathodic scan, they remain at 7.27 Å up to 0.6 V before decreasing down to initial values back to 0 V. As a matter of fact, these potential limits match the onset potentials of the two waves corresponding to the birnessite Mn^{4+}/Mn^{3+} faradic reactions at 0.60 V and 0.52 V for manganese cation oxidation and reduction, respectively (Fig. 3, black curves). This definitively confirms intercalation/deintercalation of alkali cations from the electrolyte to be associated to the charge compensation in charge–discharge redox reactions. For this reason, the higher maximum variation in *d*-spacing obtained within a cycle in LiCl is attributed to a higher insertion/extraction rate of Li^+, which provides more of pseudocapacitive contribution to the electrode [24]. In addition, the more pronounced redox peaks observed on the CV curve of MnO_2 birnessite in LiCl electrolyte (Fig. 3b, black curve) imply that the charge delivered by the intercalaction/deintercalation process of Li^+ is higher than that of K^+ cations. In contrast, Mn^{4+}/Mn^{3+} redox reactions have a limited impact on the birnessite layer structure since Mn—Mn distances remain unchanged as demonstrated by the stability of the (1 1 0) *d*-spacing at 2.48 Å all along the charge–discharge cycle.

3.4. MnO_2 H-spinel

The XRD pattern of the spinel phase (Fig. A.2) confirms the formation of the 3D tunneled cubic structure (JCPDS 44-0992) by the presence of peaks at *d*-spacings = 4.6 (1 1 1), 2.4 (3 1 1), 2.3 (2 2 2), 2.0 (4 0 0), 1.8 (3 3 1), 1.5 (5 1 1) and 1.4 Å (4 4 0). During the voltammetry cycling, the main changes in peak positions concern the (1 1 1) crystalline planes. However, (2 2 2) as well as (4 0 0) planes experience moderate peak shifts too, while (3 1 1) plane position is not affected by the charge state. The variation of the lattice spacing for the (1 1 1) reflection of MnO_2 spinel is depicted in Fig. 6 as a

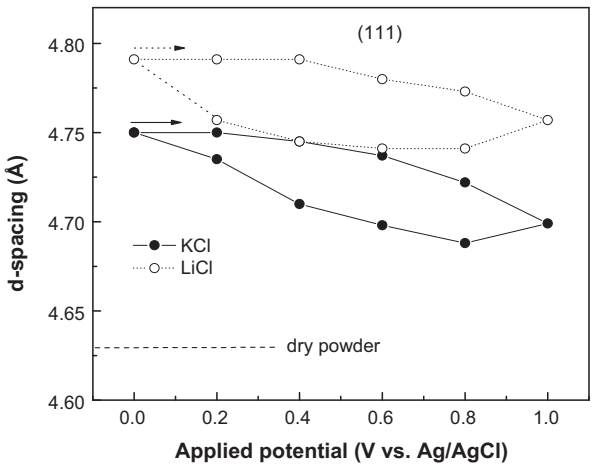

Fig. 6. Variation of the (1 1 1) Bragg peak of MnO_2 spinel-based electrode during the course of a CV scan recorded in the presence of 1 M KCl or LiCl aqueous solutions.

function of the applied potential. As for MnO_2 birnessite, immersion into LiCl or KCl electrolytes promotes drastic increases in the (1 1 1) *d*-spacing even before cycling. A similar increase is observed for other peaks of the pristine dry MnO_2 spinel. This increase of the lattice spacing demonstrates the hosting capabilities of MnO_2 spinel supported by its remarkable ionic conductivity (0.017 S cm^{-1}) [12]. As shown in Fig. 1b, the size of the structural cavities in MnO_2 spinel is about 2.9 Å, which tends to be too small in comparison to the size of hydrated $K^+(H_2O)_x$ and $Li^+(H_2O)_x$ cations as well as $Cl^-(H_2O)_x$ anions (6.3 Å). It could however accept water molecules (2.78 Å). The diffusion of alkali cations in MnO_2 spinel is only possible as desolvated species. Alkali cations are then located in Td sites but can eventually share Oh sites in a lesser extent. The size of the Td site at 1.94 Å is large enough to allow the insertion of K^+ cations (ionic radius: 1.51 Å) as well as Li^+ cations (ionic radius: 0.73 Å) [31]. MnO_2 spinel is known for its ion exchange capacity and is a remarkable host structure for alkali or alkaline-earth cations giving rise to a large family of A_xMnO_2 (A = Li, Na, K, Mg, Ca, Sr) phases of various compositions [32,33]. After immersing the as-prepared protonated spinel based electrode into the electrolyte solutions, the (1 1 1) *d*-spacing increases by +3.5% in LiCl and 2.5% in KCl (Fig. 6). These changes originate from proton to lithium and potassium ion exchanges, respectively. The exchange capacity of MnO_2 spinel towards Li^+ and K^+ depends on hydration energies of these alkali species in the aqueous phase (−511 kJ mol^{-1} and −321 kJ mol^{-1}, respectively [34]) and is obviously greater for Li^+ than for K^+ [32]. Comparatively, a larger amount of Li^+ than K^+ is inserted upon immersion in the electrolyte solutions. Alkali cation insertion causes a decrease in the water content because of H^+/A^+ ($A^+ = Li^+$ or K^+) ion exchange reaction and/or of the steric exclusion of water molecules out from the structure cavities. More interestingly, it also promotes the reduction of Mn(IV) to Mn(III) in the solid phase which is actually responsible for the observed increase in the (1 1 1) *d*-spacing since Mn—O distances, and consequently the crystal lattice, strongly depend on Mn oxidation state: *d*(Mn(III)—O) = 2.01 Å while *d*(Mn(IV)—O) = 1.91 Å [35]. The larger amount of Li^+ exchanged, compared to K^+, account for the corresponding larger (1 1 1) *d*-spacing increase.

Figs. 6 and A.5 indicate that the spinel *d*-spacing variations follow the same trend during the voltammetric cycling in the presence of KCl or LiCl solutions. The lattice spacing decreases during the anodic scan, while roughly increases during the cathodic scan to regain its initial value. During the anodic scan of the spinel electrode, the oxidation of Mn^{3+} results in the contraction of (1 1 1) planes and in a lower extent the (2 2 2) and (4 0 0) planes of the spinel phase. However, there is no obvious oxidation nor reduction peaks observed on MnO_2 spinel CV (Fig. 3, red curves) and the short plateau at the beginning of the anodic scan, up to 0.4 V in LiCl and 0.2 V for KCl in Fig. 6 could not unambiguously be associated to any Mn^{4+}/Mn^{3+} redox reactions. Origins from energy barrier of nucleation for expanded structure domain can be suggested. When the potential is swept to the cathodic direction, the structure keeps on contracting at potentials down to 0.8 V. Below this potential, the decrease of (1 1 1) *d*-spacing is characteristic of the contraction of the lattice undergoing the reduction of Mn^{4+} to Mn^{3+}. The contraction at the beginning of the cathodic scan could be associated to structural distortions along the Jahn–Teller quantification axis (very strong in Mn^{3+} system [36]) or to Mn^{3+} anti-site defects [37]. Fig. 6 indicates that the variation of lattice spacing within a cycle is fully reversible and slightly larger in aqueous KCl (0.062 Å) than in LiCl solution (0.048 Å). These weak amplitude changes, compared to those observed for MnO_2 birnessite, confirm that the maximum variation in lattice parameters is roughly independent to the size of inserted cations with respect to the size of the Td site. Nevertheless, the current intensity observed on the spinel CV curve in KCl is indeed greater than that in LiCl (Fig. 3, red curves), attesting a higher capacitance delivered in the former case. A larger capacitance in KCl than in LiCl could originate from a larger amount of Mn(III) oxidized to Mn(IV) then leading to a larger variation in the (1 1 1) *d*-spacing.

Table 1
Variations of *c* and *a* parameters for MnO_2 cryptomelane calculated from (0 0 2) and (2 0 0) *d*-spacings, respectively.

Sample type	*c* (Å)	$\Delta c/c_0$ (%)	*a* (Å)	$\Delta a/a_0$ (%)
Dry fresh powder	2.854	–	9.823	–
Fresh electrode in LiCl	2.856	−0.08	9.811	−0.12
Fresh electrode in KCl	2.852	0.08	9.823	<−0.01

c_0 and a_0 represent the cell parameters from fresh powders along *c*-axis and *a*-axis, respectively.

3.5. MnO_2 Na-cryptomelane

The cryptomelane XRD pattern (Fig. A.2) shows typical reflections of the 2 × 2 channeled MnO_2 (JCPDS 29-1020) located at *d*-spacings = 6.9 (1 1 0), 4.9 (2 0 0), 3.1 (3 1 0), 2.4 (2 1 1), 2.1 (3 0 1), 1.8 (4 1 1) and 1.4 Å (0 0 2). MnO_2 cryptomelane was prepared by thermal treatment of Na_xMnO_2-birnessite [19,38]. Its structure is formed through roughly squared channels along the *b*-axis. Those are built by 2 × 2 edge-sharing MnO_6 octahedra (Fig. 1c). The size of the channels ranges from 5.0 Å (edge) to 6.3 Å (diagonal). The in situ synchrotron XRD investigation of MnO_2 cryptomelane is based on the (0 0 2), (2 1 1), (2 0 0) and (1 1 0) reflection planes. Fig. 7 summarizes the *d*-spacings data for the as-prepared electrode cycled in LiCl or KCl solutions. After immersion into the electrolytes, the crystal structure (tetragonal) of the pristine Na-cryptomelane remains basically the same but there are slight changes in the *d*-spacing series. As shown in Table 1 and Fig. 7a, the crystallographic cell was found to enlarge slightly along the *c*-axis ((0 0 2) planes) in the presence of KCl (+0.08%) and contract of the same magnitude in the presence of LiCl solution (−0.08%). On the other hand, the *a* cell parameter (calculated from (2 0 0) *d*-spacings) contracts a bit more in LiCl solution (−0.12%) while remaining in KCl electrolyte. There is definitely an extent of ionic exchange upon immersion of the dry powder into the electrolyte. The channel dimensions are large enough to host hydrated Li^+ or K^+ (2.25 and 2.92 Å respectively) as well as water molecules (2.8 Å). For this reason, the shortening along both *a*-axis and *b*-axis by immersion in LiCl electrolyte likely results from ion exchange of Na^+ for Li^+ within the 2 × 2 cavity. Thus, the exchange process involves the diffusion of alkali cations within

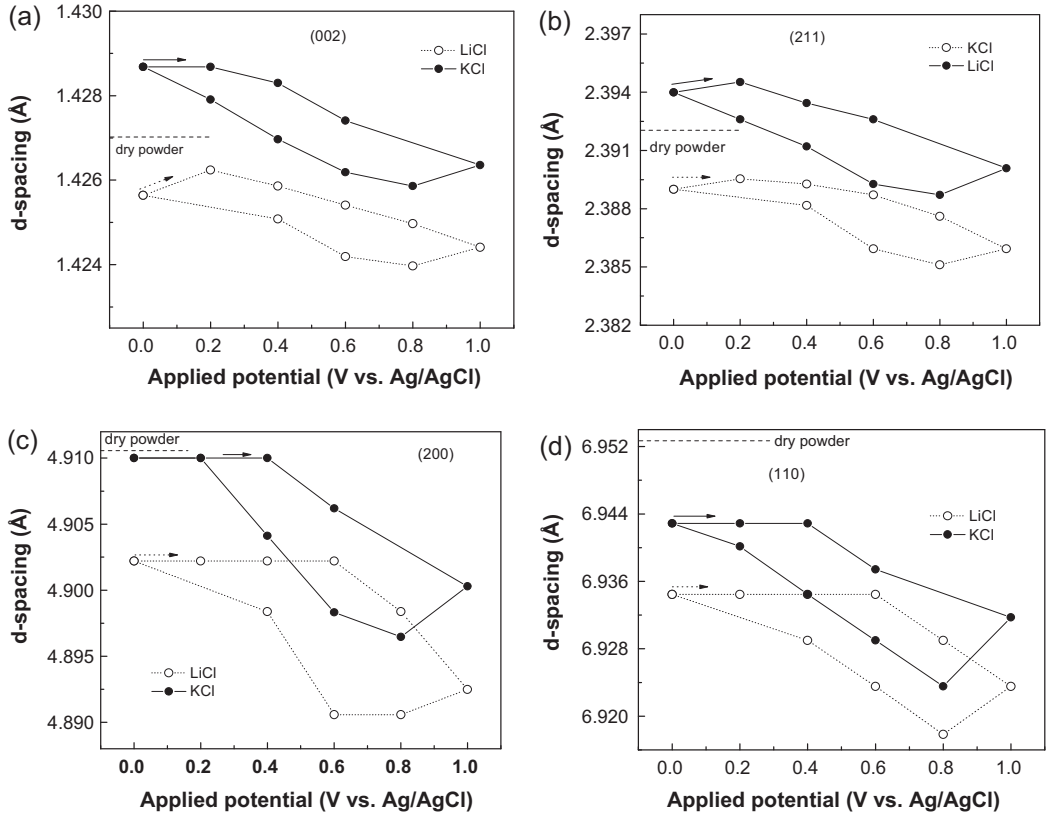

Fig. 7. Variations of (a) (0 0 2), (b) (2 1 1), (c) (2 0 0) and (d) (1 1 0) Bragg peaks of MnO_2 cryptomelane-based electrode during the course of a CV scan recorded in the presence of 1 M KCl or LiCl aqueous solutions.

the lattice and is evidenced by the consistent shortening in lattice parameters in LiCl electrolyte. In the same way, ion exchanges from Na^+ to K^+ promoted by immersion in KCl electrolyte induce the observed increase in the (2 0 0) *d*-spacing while effect on (0 0 2) *d*-spacing is rather limited.

Figs. 7 and A.6 confirm that *d*-spacings of all planes follow the same trend: they typically increase during the cathodic scan, while decrease during the anodic scan. However, some exceptions occur upon potential reversal. For example, the *d*-spacing decreases rather than increases when the potential scan is switched from being anodic to cathodic within 1.0–0.8 V. On the other hand, the *d*-spacing increases or remains unchanged rather than decreases when the potential change from 0.0 V to 0.2 V. Overall, all these irregular trends occurring at the potential ends cause large hysteresis in *d*-spacing for all crystal planes during the cycling.

The "breathing" process of the cryptomelane structure is obviously more complex than either birnessite and spinel MnO_2 phases. Fig. 7a and b demonstrates that (0 0 2) and (2 1 1) planes firstly expand from 0 to 0.2 V and then contract during the anodic scan. During the cathodic scan, these processes are inversed since the contraction occurred in a first step. For the (1 1 0) and (2 0 0) reflections (Fig. 7c and d), both associated to *a* (and *b*)-axis, only a contraction occurs during the anodic scan since corresponding *d*-spacings remain unchanged until above 0.4–0.6 V. This potential region corresponds to major increases of the anodic current in the cryptomelane CV curves (Fig. 3, blue curves). A similar phenomenon was also observed for the birnessite-based electrode along the *c*-axis (Fig. 4). Intercalation/deintercalation of alkali cations from the electrolyte, associated to the charge compensation in charge–discharge redox reactions, can reasonably be pointed out [39]. When the potential is reversed to the cathodic direction, the cryptomelane contraction continues until 0.8–0.6 V, where the swelling process begins. Likewise MnO_2-spinel, this "extra" contraction could be associated to Jahn–Teller induced structural distortions. At the end of the cathodic scan, the (1 1 0) and (2 0 0) planes regain their initial *d*-spacings. The extent of lattice parameter variations reach 0.25–0.28% during cycling in KCl, which is more than two times (0.12%) that resulting from the ionic exchange (immersion) in LiCl. Such a behavior results from a larger capacitance in KCl than in LiCl, as evidenced by the CV data (Fig. 3, blue curves). Accordingly, the charge storage mechanism observed in this material likely involves bulk insertion/deintercalation of alkali cations.

3.6. MnO_2 OMS-5

The formation of Na-OMS-5 phase is confirmed by the XRD pattern shown in Fig. A.2 with diffraction peaks at *d*-spacings = 7.0 (2 0 0), 5.8 (0 0 4), 3.4 (4 0 0), 3.3 (4 0 2), 2.5 (3 1 1), 2.3 Å (6 0 0) [40]. The structure is built through 2×4 channels of rectangular shape with $L = 9.9$ Å and $l = 5.4$ Å, at first sight large enough to host LiCl as well as KCl electrolyte species. Fig. 8 depicts the increase of the (0 0 2) and (2 0 0) *d*-spacings, along *c*- and *a*-axes respectively, after immersing the as prepared Na-OMS-5-based electrode into LiCl or KCl solutions (Fig. 1f). The electrode immersion directly impacts on the channel size since (0 0 2) *d*-spacing corresponds to the largest section, *L*, of the channel while (2 0 0) peak corresponds to the lowest section, *l*. The same increase (+1.1%) is measured for the (0 0 2) *d*-spacing in the presence of both electrolyte solutions (Fig. 8a) demonstrating a limited size effect thanks to the large *L* dimension towards $Li(H_2O)_x^+$, $K(H_2O)_x^+$ or water molecules. In contrast, the (2 0 0) *d*-spacing increases by +1.7% and +1.2% in LiCl and KCl solutions, respectively (Fig. 8b). Likewise MnO_2-birnessite, the higher increase reached in LiCl suggests a better ion exchange capability

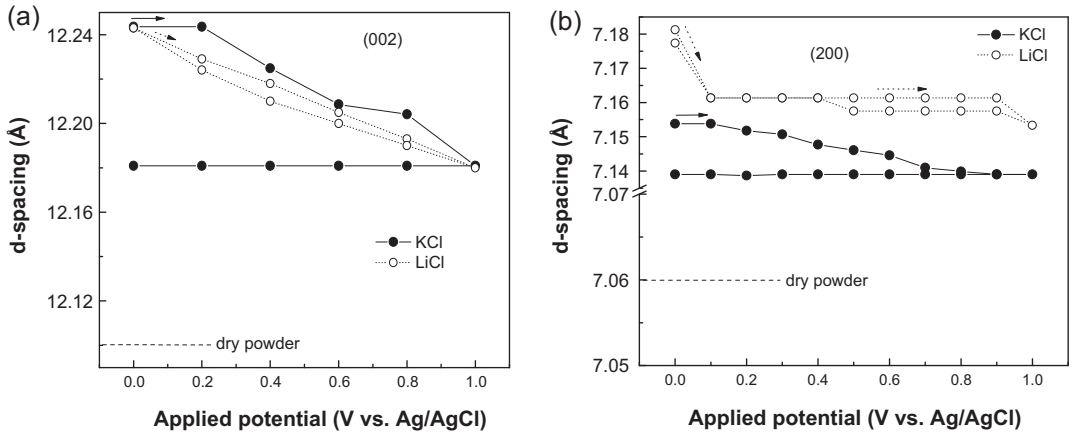

Fig. 8. Variation of (a) (0 0 2) and (b) (2 0 0) Bragg peaks of MnO_2 OMS-5-based electrode during the course of a CV scan recorded in the presence of 1 M KCl or LiCl aqueous solutions.

of OMS-5 towards Li^+ than K^+. The increases of *d*-spacings upon the electrode immersion however confirm the ability of OMS-5 to accommodate hydrated alkali cations in the large 2×4 channels, as supported by its relevant ionic conductivity at $0.02\,S\,cm^{-1}$ (the highest in the studied MnO_2 allotropes [12]). It should be noticed that the swelling of 2×4 channels observed in the presence of KCl is almost the same along the I or *L* channel section (+1.2 vs. +1.1%). However, in the presence of LiCl, the intercalation process of Li^+ hydrated cations imposes a larger constraint in the smallest channel section, *l*, than in the largest section, *L* (+1.7 vs +1.1%) which accommodates species intercalation more easily. For both (0 0 2) and (2 0 0) reflection planes, *d*-spacings decrease when the potential is swept in the anodic direction (Fig. A.7). As for MnO_2-cryptomelane, this behavior results from the deintercalation of alkali cations during the oxidation of Mn^{3+} to Mn^{4+}. The maximum variations for the (0 0 2) reflection plane are estimated at 0.52% in the presence of LiCl and KCl. For the (2 0 0) reflection plane, the maximum variations are about 0.42 and 0.20% in LiCl and KCl solutions, respectively. This discrepancy in *L* and *l* changes demonstrates an anisotropic distortion of the channel during charge/discharge. Surprisingly, the changes of the 2×4 OMS-5 cavity are more important following its large width, *L*, rather than its short one, *l*. In LiCl solution, the (0 0 2) *d*-spacing continually decreases during the entire anodic scan (Fig. 8a), while the (2 0 0) *d*-spacing remains the same in the 0.1–0.9 V range: cation desintercalation mostly affect the channel size in its largest section. While the structural changes are fully reversible in LiCl (Fig. A.7b and d), irreversible changes in lattice parameters occur when the electrode is cycled in KCl (Fig. A.7a and c). Here again size effects are pointed out: thank to their small size $Li^+(H_2O)_x$ cations are easily and reversibly intercalated into the structure all over the charge/discharge process. In contrast, in KCl, unexchanged hydrated sodium cations [19,38] are deintercalated from the cavity of the pristine OMS-5 during the first oxidation step (anodic scan), while $K^+(H_2O)_x$ are not inserted during the subsequent reduction step (cathodic scan). This behavior may be explained by the larger size of $K^+(H_2O)_4$ (2.92 Å) and despite the cavity sizes of MnO_2 OMS-5 (Fig. 1f). This latter point explain the discrepancies upon immersion of the OMS-5 based electrode in LiCl and KCl: as hydrated Na^+ are fully exchanged by $Li^+(H_2O)_x$ inside the cavities thanks to the ion exchange capabilities of OMS-5, immersion in KCl only promotes the hydration of Na^+ without any exchange.

Although for both cryptomelane and OMS-5, charge/discharge processes involve intercalation/deintercalation of hydrated electrolyte cations into/from their 1D channels, the observed irreversibility in the case of OMS-5 operated in KCl electrolyte points out the main difference between these two MnO_2 phases: despite a larger, and eventually more flexible cavity, OMS-5 cannot accommodate $K^+(H_2O)_x$ size while cryptomelane easily does. On the other hand, the relatively low current intensities of redox waves observed on the CV curve of MnO_2 OMS-5 (Fig. 3, purple curves) does not allow any structural relationship between the deintercalation/insertion process and the oxidation/reduction of Mn^{3+}/Mn^{4+}.

4. Conclusions

Despite electrochemical performances of roughly the same level, the four studied MnO_2 allotropes display distinct charge storage mechanisms closely related to their structural arrangement. As evidenced by in situ synchrotron XRD measurements, a specific "breathing" of each MnO_2 structure occurs upon charge/discharge cycling and mechanisms all involve Mn(III)/Mn(IV) redox reactions inducing (i) electrolyte cation intercalation/deintercalation or insertion/desinsertion for charge compensation and (ii) metal—oxygen bond distance changes. For the 2D MnO_2-birnessite, the structural breathing in the *c*-axis direction comes from the modulation of the electrostatic interaction between negatively charged layers and intercalated hydrated cations from the electrolyte. Drastic changes in the compact 3D structure of MnO_2-spinel are induced by Mn(III)/Mn(IV) redox reaction through changes in metal—oxygen bond length. In contrast, dehydrated electrolyte cations lying in the Td sites have limited structural impact. For MnO_2-cryptomelane as well as for MnO_2-OMS-5, charge compensations proceed by intercalation/deintercalation of hydrated cations in the 1D channels driven by size/steric considerations.

Acknowledgments

The authors thank the Centre National de la Recherche Scientifique (CNRS) and the Agence Nationale de la Recherche (ANR) for financial support through the ABHYS project and Marie-Liesse Doublet (ICGM) for the helpful discussions.

Appendix A. Supplementary data

Supplementary data associated with this article can be found, in the online version, at doi:10.1016/j.jpowsour.2012.01.103.

References

[1] J.J. Yoo, K. Balakrishnan, J. Huang, V. Meunier, B.G. Sumpter, A. Srivastava, M. Conway, A.L.M. Reddy, J. Yu, R. Vajtai, P.M. Ajayan, Nano Lett. 11 (2011) 1423–1427.
[2] P.-C. Chen, G. Shen, Y. Shi, H. Chen, C. Zhou, Nano ACS 4 (2010) 4403–4411.
[3] G.-R. Li, Z.-P. Feng, Y.-N. Ou, D. Wu, R. Fu, Y.-X. Tong, Langmuir 26 (2010) 2209–2213.
[4] D. Hulicova-Jurcakova, A.M. Puziy, O.I. Poddubnaya, F. Suărez-García, J.M.D. Tascön, G.Q. Lu, J. Am. Chem. Soc. 131 (2009) 5026–5027.
[5] M. Toupin, T. Brousse, D. Bélanger, Chem. Mater. 16 (2004) 3184–3190.
[6] S.-L. Kuo, N.-L. Wu, J. Electrochem. Soc. 153 (2006) A1317–A1324.
[7] P. Ragupathy, H.N. Vasan, N. Munichandraiah, J. Electrochem. Soc. 155 (2008) A34–A40.
[8] Y. Lei, C. Fournier, J.-L. Pascal, F. Favier, Microporous Mesoporous Mater. 110 (2008) 167–176.
[9] S. Devaraj, N. Munichandraiah, J. Phys. Chem. C 112 (2008) 4406–4417.
[10] T. Shinomiya, V. Gupta, N. Miura, Electrochim. Acta 51 (2006) 4412–4419.
[11] J.O. Besenhard, Handbook of Battery Materials, Wiley VCH Verlag, Weinheim, Germany, 1999, pp. 85–133.
[12] O. Ghodbane, J.-L. Pascal, F. Favier, ACS Appl. Mater. Interf. 1 (2009) 1130–1139.
[13] T. Brousse, M. Toupin, R. Dugas, L. Athouel, O. Crosnier, D. Bélanger, J. Electrochem. Soc. 153 (2006) A2171–A2180.
[14] L. Athouël, F. Moser, R. Dugas, O. Crosnier, D. Bélanger, T. Brousse, J. Phys. Chem. C 112 (2008) 7270–7277.
[15] M. Nakayama, S. Konishi, H. Tagashira, K. Ogura, Langmuir 21 (2005) 354–359.
[16] M. Nakayama, H. Tagashira, Langmuir 22 (2006) 3864–3869.
[17] S.C. Pang, M.A. Anderson, T.W. Chapman, J. Electrochem. Soc. 147 (2000) 444–450.
[18] X.-F. Shen, Y.-S. Ding, J. Liu, J. Cai, K. Laubernds, R.P. Zerger, A. Vasiliev, M. Aindow, S.L. Suib, Adv. Mater. 17 (2005) 805–809.
[19] R.M. McKenzie, Miner. Mag. 38 (1971) 493–502.
[20] F. Cheng, Y. Su, Z. Liang, Z. Tao, J. Chen, Chem. Mater. 22 (2010) 898–905.
[21] W. Xiao, D. Wang, X.W. Lou, J. Phys. Chem. C 114 (2010) 1694–1700.
[22] I. Roche, K. Scott, J. Appl. Electrochem. 39 (2009) 197–204.
[23] S. Wen, J.W. Lee, I.H. Yeo, S. Park, S. Mho, Electrochim. Acta 50 (2004) 849–855.
[24] A. Yuan, Q. Zhang, Electrochem. Commun. 8 (2006) 1173–1178.
[25] M. Manickam, P. Singh, T.B. Issa, S. Thurgate, R.D. Marco, J. Power Sources 130 (2004) 254–259.
[26] H. Ohtaki, T. Radnai, Chem. Rev. 93 (1993) 1157–1204.
[27] Q. Feng, H. Kanoh, Y. Miyai, K. Ooi, Chem. Mater. 7 (1995) 1226–1232.
[28] H. Kanoh, W. Tang, Y. Makita, K. Ooi, Langmuir 13 (1997) 6845–6849.
[29] P. LeGoff, N. Baffier, S. Bach, J.P. Pereira-Ramos, Mater. Res. Bull. 31 (1996) 63–75.
[30] K.S. Abou-El-Sherbini, M.H. Askar, R. Schöllhom, Solid State Ionics 150 (2002) 407–415.
[31] F.A. Cotton, G. Wilkinson, C.A. Murillo, M. Bochmann, Advanced Inorganic Chemistry, sixth ed., John Wiley and Sons, New York, Chichester, 1999.
[32] K. Ooi, Y. Miyai, S. Katoh, Solvent Extr. Ion Exch. 5 (1987) 561–572.
[33] K. Ooi, Y. Miyai, J. Sakakihara, Langmuir 7 (1991) 1167–1171.
[34] G. Wulfsberg, Principles of Descriptive Chemistry, Brooks/Cole Publishing, Monterey, CA, 1987.
[35] A. Paolone, C. Castellano, R. Cantelli, G. Rousse, C. Masquelier, Phys. Rev. B 68 (2003) 014108–14115.
[36] A. Yamada, M. Tanaka, K. Tanaka, K. Sekai, J. Power Sources 73 (1999) 81–82.
[37] M. Cheah, P.J. Saines, B.J. Kennedy, J. Solid State Chem. 179 (2006) 1775–1781.
[38] O. Ghodbane, J.-L. Pascal, B. Fraisse, F. Favier, ACS Appl. Mater. Interf. 2 (2010) 3493–3506.
[39] M. Nakayama, A. Tanaka, Y. Sato, T. Tonosaki, T. Ogura, Langmuir 21 (2005) 5907–5913.
[40] Z.H. Liu, K. Ooi, Chem. Mater. 15 (2003) 3696–3703.